Effect of diffusion on impedance measurements in a hydrodynamic flow focusing sensor†

Mansoor Nasir,[a] Dorielle T. Price,[b] Lisa C. Shriver-Lake[a] and Frances Ligler*[a]

Received 28th April 2010, Accepted 26th July 2010
DOI: 10.1039/c005257d

This paper investigated the effects of diffusion between non-conductive sheath and conductive sample fluids in an impedance-based biosensor. Impedance measurements were made with 2- and 4-electrode configurations. The 4-electrode design offers the advantage of impedance measurements at low frequencies (<1 kHz) without the deleterious effects of double layer impedance which are present in the 2-electrode design. Hydrodynamic flow focusing was achieved with a modified T-junction design with a smaller cross-section for the sample channel than for the focusing channel, which resulted in 2D focusing of the sample stream with just one sheath stream. By choosing a non-conductive sheath fluid and a conductive sample fluid, the electric field was confined to the focused stream. In order to utilize this system for biosensing applications, we characterized it for electrical and flow parameters. In particular, we investigated the effects of varying flow velocities and flow-rate ratios on the focused stream. Increasing flow-rate ratios reduced the cross-sectional area of the focused streams as was verified by finite element modeling and confocal microscopy. Antibody mediated binding of *Escherichia coli* to the electrode surface caused an increase in solution resistance at low frequencies. The results also showed that the diffusion mass transport at the interface of the two streams limited the benefits of increased flow focusing. Increasing flow velocities could be used to offset the diffusion effect. To optimize detection sensitivity, flow parameters and mass transport must be considered in conjunction, with the goal of reducing diffusion of conducting species out of the focused stream while simultaneously minimizing its cross-sectional area.

Introduction

Despite the development of biosensors for applications ranging from medicine to food and water safety[1,2] and from environmental monitoring[3] to detection of biochemical warfare agents,[4] only a few of these biosensors rely on micron-scale fluidics.[5] While smaller channel dimensions can improve sensitivity, expedite biochemical reactions, decrease reagent costs, and facilitate automation, the complex real-world samples can clog small channels. Hydrodynamic focusing addresses this problem by using laminar flow streams to provide virtual channels with flexible interfaces that can be much smaller than the physical dimensions of the solid channel. The inherent lack of convective mixing means that one fluidic stream can be used to shape and focus another fluidic stream.[6] Designs of varying complexity have been described in the literature to focus a sample stream from one, two, three or four sides.[7–10]

Biosensors employing hydrodynamic focusing have been reported for cell or particle detection,[11] cytometry,[12,13] sorting[14] and mixing applications.[15,16] Most incorporate optical analysis, usually fluorescence, for increased sensitivity and specificity. However, such systems include bulky optical components which are not easily integrated into lab-on-a-chip systems.[17] An alternative is to achieve target detection of species with techniques based on measurement of electrical signal, especially impedance.

Impedance techniques have an established history in the field of biodetection and biomonitoring with the early work by Fricke[18] and Schwan and Cole[19] dating back to the early part of the twentieth century. Later research focused on use of impedance spectroscopy for detection of bacteria,[20] Coulter counters[21] and analysis of cell morphology, mobility and density.[22] More recently, impedance measurement techniques have been incorporated in hydrodynamic flow-focusing devices for biodetection purposes[23–26] and flow cytometry.[27–29] Impedance measurements have been made with 4- and 2-electrode configurations, with each configuration providing unique information about the cell–electrode–electrolyte system. In 2-electrode measurements, current is passed between the same pair of electrodes as is used for the voltage measurement. Two-electrode measurements are very sensitive to changes at the electrode interface, but the formation of electrical double layer and other parasitic capacitances means that low frequency measurements are difficult with this setup.[30–32] In a 4-electrode system an oscillating signal is applied between the two outer electrodes and the impedance is measured across the two inner electrodes. Physical separation of the current and sensing electrodes in the 4-electrode configuration results in reduced parasitic double layer impedance, especially at lower frequencies.[33] Most impedance based biosensors in the literature use the 2-electrode configuration and only a few 4-electrode based systems have been reported.[10,33,34]

[a]*Center for Bio/Molecular Science and Engineering, Naval Research Laboratory, 4555 Overlook Avenue SW, Washington, DC, 20375, USA. E-mail: frances.ligler@nrl.navy.mil*
[b]*BioMEMS and Microsystems Laboratory, Dept. of Electrical Engineering, University of South Florida, 4202 East Fowler Avenue, ENB 118, Tampa, FL 33620, USA*

† Electronic supplementary information (ESI) available: Equivalent electrical model for 2 and 4 electrode configurations. Live/dead strain to confirm cell viability. See DOI: 10.1039/c005257d

We have previously described and characterized a simple 1D flow-focusing sensor that was used to measure changes in voltage due to the presence of conducting particles.[34] Here we describe a simple flow-focusing design that used one sheath stream to focus a sample stream in 2D. By increasing the sheath-to-sample flow-rate ratio (FRR), the sample stream was focused along the sensing surface. Sensing was achieved using 2 and 4-electrode configurations, the latter of which reduced the double layer effects, thus making it possible to measure impedance at low frequencies. We applied an oscillating input voltage signal (1 kHz frequency) to the outer two electrodes while the impedance measurements were made with the two inner electrodes. By choosing the sheath fluid to be non-conductive (deionized water) and the sample a conducting fluid (phosphate buffer saline or PBS), the injected current was confined to the focused stream. In the process of characterizing the hydrodynamically focused conducting stream, we identified factors that affected the cross-section of the confined layer using numerical simulations, confocal microscopy and impedance measurements. Our results also indicated that the diffusion between the sheath and sample fluids due to diffusion mass transport became significant as the focused layer cross-section decreased, and this caused appreciable changes in bulk impedance baseline measurements. Bacterial cells were bound by antibodies on the electrodes, and the change in impedance was demonstrated with the 2 and 4-electrode configurations. The results highlight the importance of evaluating flow, mass transport and electric field confinement parameters in optimizing the detection sensitivity of hydrodynamic focusing devices.

Theory

Flow in channels can be characterized by certain dimensionless numbers which specify the flow regime as well as the relative importance of diffusive or convective mass transport. Reynolds number *Re* is the ratio of inertial forces to viscous forces and is given by

$$Re = \frac{VL}{\nu} \tag{1}$$

where ν is the kinematic fluid viscosity, V is the fluid velocity, and L is the characteristic distance, which for rectangular channels is given by: 4 × area/perimeter. The typical values of *Re* for flow in microchannels are less than 100 and signify that the flow is predominantly laminar in nature.[35] Under laminar flow conditions, mixing is generally due to diffusion and not convection. This behavior is characterized by the Péclet number given by

$$Pe = \frac{UH}{D} \tag{2}$$

where U is the average flow rate, D is the diffusion coefficient and H is the characteristic length of the system perpendicular to the direction of the flow, which in this case is the height of the focused stream. When the Péclet numbers are high, mass transfer is mainly due to convective bulk transport of liquid instead of transfer by molecular diffusion.[36]

Under laminar flow conditions, fully developed flow between two infinite parallel plates with no-slip condition at the walls is essentially 2D and has a parabolic profile with maximum velocity v_{max} at the center of the plates. The velocity v_x in the flow direction at any point at a distance of y from the center of the channel is given by

$$v_x(y) = v_{max}\left(1 - \frac{y^2}{w^2}\right) \tag{3}$$

where w is the distance from the center to either plate. For flow between parallel plates, also called Poiseuille flow, v_{max} is 3/2 times the average velocity calculated based on the channel cross-section and total flow rates.[37]

Interfacial impedance

The gold electrodes in this system are considered completely polarizable and thus pass no faradaic current. In addition, impedance measurements are performed with a small AC signal applied at equilibrium; thus the response is linear, and no charge-transfer reactions occur within the electrochemical system. When the electrodes are in contact with the liquid electrolyte, the electrodes attract ions and form a double layer across the electrode/electrolyte interface with a thickness on the order of angstroms. The double layer consists of a layer of ions that are specifically adsorbed to the surface of the electrodes and a diffuse layer, in which ions are dispersed perpendicularly away from the electrode surface due to thermal motion. The thickness of the diffuse layer increases in more dilute solutions. Since the adsorbed (ads) and diffuse (diff) layers are in series, the equivalent double layer (dl) capacitance can be described by the following equation

$$\frac{1}{C_{dl}} = \frac{1}{C_{ads}} + \frac{1}{C_{diff}} \tag{4}$$

At sufficiently high conductivities of electrolytes the thickness of the diffuse layer decreases (C_{diff} increases) and $C_{dl} \approx C_{ads}$.[38] The typical values are in the range of 10 to 40 μF cm^{-2}.[39,40] In 2-electrode configurations, in the absence of any faradaic processes, the equivalent impedance is thus described by the series combination of double layer capacitance and solution (bulk) resistance (see ESI†). The corresponding double layer impedance Z_{dl} is inversely proportional to capacitance as described by

$$Z_{dl} = \frac{1}{j\omega C_{dl}} \tag{5}$$

where j is the standard imaginary unit with the property $j^2 = -1$ and ω is angular frequency. Thus as the electrode area increases, the double layer capacitance increases and in turn the impedance decreases. For 4-electrode configurations, the contribution of the double layer capacitance is negligible and equivalent impedance is found by a parallel combination of bulk resistance and capacitance (see ESI†).

Bulk impedance

Bulk resistance for coplanar electrodes is given by

$$R_{bulk} = \rho\kappa \tag{6}$$

where ρ is the measured resistivity of the focused stream, κ is geometric factor called the cell constant. This equation holds for

the 2- and 4-electrode systems although the expression for cell constant is different in each case.

The bulk capacitance of the 4-electrode system is inversely proportional to its cell constant. The cell constant of the 4-electrode configuration can be estimated using a point-electrode model shown in Fig. 1. The model consists of four electrodes that are located on the surface of the glass slide. The electrodes are in contact with the focused sample stream of thickness z which is sandwiched by the sheath stream from the top. The resistivity of glass ρ_{glass} is assumed to be infinite for the purpose of this model.

Using the imaging method the cell constant can be approximated to the first order by[41]

$$\kappa_{4pt} = \frac{1}{\pi}\left[\frac{b}{a(a+b)} + 2\Gamma\left(\frac{1}{\sqrt{a^2+4z^2}} - \frac{1}{\sqrt{(a+b)^2+4z^2}}\right)\right] \quad (7)$$

where a is the distance between current and sense electrodes and b is the distance between sense electrodes. The interface between the high conductivity focused stream and low conductivity sheath stream is seen as a semi-transparent mirror having a reflection coefficient Γ defined as[42]

$$\Gamma = \frac{\rho_2 - \rho_1}{\rho_2 + \rho_1} \quad (8)$$

where ρ_1 and ρ_2 are the resistivities of sample and sheath fluids respectively. In an aqueous solution, there is also a capacitive pathway for the current, which can be modeled as a capacitor in parallel with the resistance of the sample. The bulk capacitance is given by[43]

$$C_{bulk} = \frac{\varepsilon_0 \varepsilon_r}{\kappa_{4pt}} \quad (9)$$

where ε_0 is the permittivity of vacuum and ε_r is the relative permittivity of the conductive PBS. The permittivity of ionic solutions is inversely proportional to conductivity and approaches the permittivity of water (~78) as the conductivity decreases.[44,45] For the frequency range (<1 kHz) used in our data, the permittivity can be assumed to be constant.[44] From eqn (6) and (7) it can be seen that as the thickness of the focused stream decreases, the resistance increases while eqn (9) suggests that bulk capacitance decreases as the focused layer thickness decreases. The cell constant for a 2-electrode model has been found using conformal mapping techniques elsewhere.[43,46]

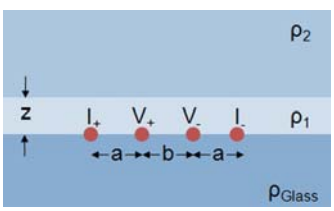

Fig. 1 A point-electrode model for the tetrapolar configuration where the current is injected in the outer two electrodes and voltage is sensed from the inner two. The distance between current and sense electrodes is a and between sense electrodes is b. The conductive focused stream with resistivity ρ_1 has a height x. The non-conductive sheath with resistivity ρ_2 extends infinitely above the focused stream in this model.

Methods and materials

Electrode fabrication

Standard photolithography techniques were used to fabricate the electrodes. Borosilicate glass microscope slides (Daigger, Vernon Hills, IL) were used as the substrates. The slides had been thoroughly cleaned to allow good adhesion of electrodes to the glass surface. The slides were initially cleaned with HCl : MeOH 1 : 1 v/v for 30 minutes and then rinsed with water.

This was followed by immersion in H_2SO_4 for 30 minutes and then rinsing in water. Finally, the slides were placed in 100 °C water for 10 minutes and dried with nitrogen. Clean slides were dehydrated on a 150 °C hotplate for 5 minute and subjected to O_2 plasma for 4 minutes just before the photolithography step. A 1 μm thick layer of negative photoresist (NR7 1000PY-Futurex, Franklin, NJ) was patterned using a transparency mask (Pageworks, Boston, MA). An electron beam evaporator was used to deposit a film of gold (300 nm) onto the slides with a thin film of titanium (30 nm) as the adhesion layer. The electrodes were defined by photoresist lift-off in acetone. The current electrodes were 1000 μm wide while the widths of the sense electrodes and the inter-electrode distances were both 500 μm. A schematic of the electrode device is shown in Fig. 2a.

Microchannel

The microchannel design used in this study had two inlets for the sheath and sample fluids and one outlet. The sheath inlet

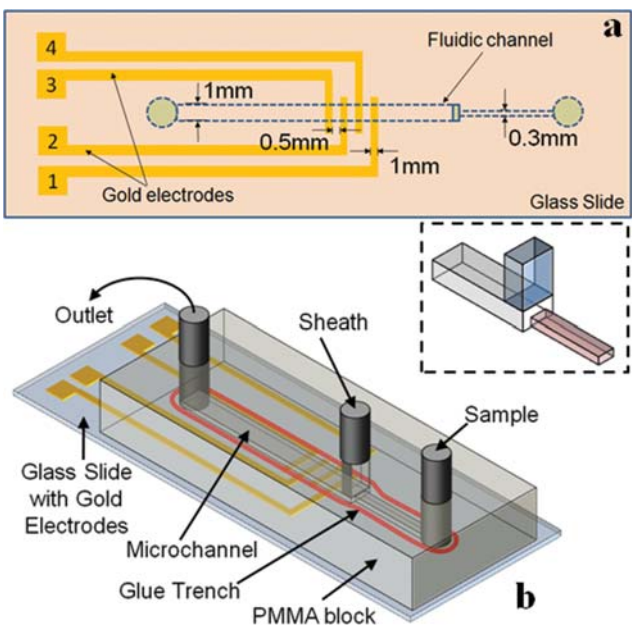

Fig. 2 (a) A top-view schematic of the gold electrodes and microfluidic channel, along with their corresponding dimensions. Outer electrodes (1 and 3) supply current while the inner two (2 and 4) sense the signal. The width of the sensing electrodes as well as the spacing between them is 0.5 mm while the current electrodes are 1 mm wide. The sample channel width is 0.3 mm which increases to 1 mm in the focusing channel. (b) Figure of an assembled microchannel and electrodes. The channel machined in PMMA is glued to the glass slide using UV curable glue. The inset shows the channel junction where sheath and sample streams meet.

(0.5×1 mm^2) was oriented at 90° with respect to the sample and focusing channels. The sample channel had a smaller cross-section (0.15×0.3 mm^2) than the focusing channel (0.25×1 mm^2); the sheath fluid focused the sample from the sides as well as the top with this geometry. The length of the channel from the sample inlet to the outlet was 30 mm.

The devices were milled from polymethylmethacrylate (PMMA) (Plexiglas G, Atofina Chemical, Inc., Philadelphia, PA) using a HAAS Mini Mill (HAAS Automation, Inc., Oxnard, CA). The sheath inlet and the focusing channel were machined with a 0.01 in (0.254 mm) long-reach endmill, and a 0.031 in (0.787 mm) endmill respectively. The sample channel was machined with a 0.01 in (0.254 mm) endmill (Harvey Tool, Rowley, MA). A 0.5 mm wide trench was milled around the microchannel and inlets using a 0.015 in (0.381 mm) endmill. This trench prevents the glue from running into the microchannel.[47] A bench top drill press was used to widen the upper half of the inlets and outlet where 0.58 mm wide metal tubing was inserted and glued into place using 5 minute epoxy (Devcon, Danvers, MA). The PMMA pieces with milled microchannels and metal tubing were glued to the microscope slides with prepared electrodes and antibodies using UV-curable adhesive (Optical adhesive #72, Norland Products, Cranbury, NJ). Fig. 2b shows the representation of a fully assembled device.

Immobilization chemistry

The electrode patterned slides were cleaned with O_2 plasma for 2 minutes prior to protein immobilization. To immobilize the antibody directly onto the gold electrode, the procedure used by Chatrathi *et al.* was employed.[48] Briefly, 250 μg of goat anti-*Escherichia coli* antibody (2 mg mL^{-1} in PBS, Fitzgerald Industries International, Concord, MA) were incubated with 40 μL 20 mM sulfo-LC-SPDP (Pierce, Rockford, IL) for 60 min at room temperature with mixing. To the mixture, 150 mM DTT in acetate buffer pH4.5 were added and incubated with mixing for 30 min. The entire mixture was then exposed to the gold electrodes for 60 min. The slides were rinsed with water, dried, and stored at 4 °C until use.

E. coli assay preparation

The cells used for this study were *E. coli* rosetta and were cultured in LB broth with 1% glucose and 0.1% ampicillin. For the assays, 1.5 mL of cell culture was spun down in an Eppendorf tube at 3000 rpm for 5 min. The supernatant was removed and 1 mL 50 mM borate buffer pH 8.0 was added to the cells. A tube of Cy3 monoreactive succinimide ester (GE Healthcare, Piscataway, NJ) was dissolved in 50 μL DMSO. Fifteen microlitres of the dye were added to the cell solution and the sample was incubated for 30 min at room temperature in the dark with shaking. The cells were respun and the supernatant was removed. The cells were washed 3 times with PBS pH 7.4 (Sigma Chemical, St Louis, MO) and stored in 1 mL PBS at 4 °C until use. The cells were used within 24 hours. Cell concentrations were typically around 10^9 cfu mL^{-1}.

Live/dead staining

To establish the viability of the cells, the impermeability of the cell membranes was tested using dye exclusion. Live/dead staining was performed using Invitrogen BacLight™ Bacterial Viability Kit L13152 (Life Technologies Corp., Carlsbad, California) to ensure the viability of the *E. coli* (see ESI†). A 1 mL cell suspension of *E. coli* cells in PBS was mixed with the stain and incubated at room temperature in the dark for 15 minutes. A 10 μL sample of the stained cells was placed on a microscope slide and a cover glass was placed on top. The cells were imaged immediately with a Nikon microscope using a 20× objective. ImageJ software (NIH, Bethesda, MD) was used to count the number of viable cells.

Flow simulations

Finite element modeling of the channels was performed using the COMSOL Multiphysics finite element analysis package (COMSOL Inc., Palo Alto, CA). The channel dimensions in the model were chosen to be identical to the ones used in the experiments. However, in order to reduce computation time, only half of the width of the channel was used in simulations, assuming channel symmetry.

Relative sample and sheath flow rates were varied to simulate changing cross-sectional area of the focused stream. The simulations were conducted in two steps. In the first step, the flow model was solved for incompressible flow. A zero-slip velocity boundary condition was assumed on the channel walls. The inlet boundary conditions were specified by the desired volumetric flow rate, and outlet boundary conditions were fixed at atmospheric pressure. Flow in the inlets was specified to be fully developed. After the velocity field was determined, the second step simulated mass transport to provide the concentration distribution, assuming a diffusion coefficient typical of a low molecular weight solute (1×10^{-9} m^2 s^{-1}). The presence of conducting ions in sample stream had an initial concentration of 1 in the diffusion/convection simulation. Similarly, the initial concentration of the sheath stream, which was devoid of ions, was chosen to be 0. An automesh with tetrahedral elements was used for all simulations. In order to accurately resolve the mass transport along the interface between the sheath and sample streams, adaptive meshing was used to increase mesh density in subsequent simulations. The mesh refinement process was repeated until no change in results was observed (*h*-method). Furthermore, the total flux in and out of the channel was compared to verify the mass balance. It was assumed that there were no chemical reactions and that the ionic nature of the sample does not effect the outcome of simulations; therefore the only factors affecting the distribution of the model species were diffusion and convection. The details of the multiphysics modules and the equations used to define flow and mass transport characteristics were previously described.[34]

Confocal microscopy

Visualization of flow focusing in the channel was performed using a Nikon Eclipse TE2000-E inverted microscope equipped with a Nikon D-Eclipse C1si confocal spectral imaging system (Nikon, Japan). Confocal images were obtained by scanning in the region downstream from where the sheath and sample streams intersect. The hydrodynamic focusing experiments were performed using de-ionized water for the sheath flow and

de-ionized water mixed with FWT Red Powder fluorescent dye (Bright Dyes, Miamisburg, OH) for visualization of the flow from sample stream inlet.

A dual syringe pump (Harvard Apparatus Model 33) provided precise control of the flow rates and flow-rate ratios. Confocal microscopy was performed using a 10× objective (NA 0.45, WD 4.00 Dry). Image resolution was 512 × 512 pixels, with a *Z*-step size spacing of 5 μm and a pixel dwell time of 7.06 μs. A 40 mW argon laser was used at the 514.5 nm excitation line, and the spectral detector of the confocal imaging system was set to detect emission between 583 and 593 nm. Image stacks were rendered and analyzed in three-dimensions using NIS-Elements AR confocal image processing software (Nikon, Japan).

Electrical impedance measurements

An Agilent 4284A LCR meter was used to perform all 2- and 4-electrode impedance measurements using a 10 mV, 1 kHz signal. For the 2-electrode system, the current was applied and the response was measured from the inner two electrodes. Baseline measurements were performed after bovine serum albumin (BSA) was passed through the channel to prevent nonspecific binding. Phosphate buffer solution (PBS) with a conductivity of 12.8 mS cm^{-1} was used as the sample fluid, and deionized (DI) water with a conductivity of 0.08 mS cm^{-1} was used as the sheath fluid. Impedance data were collected at different sheath-to-sample flow-rate ratios (FRRs) and flow velocities. In order to increase the focusing, the FRR was increased by increasing the sheath flow rate while the sample flow rate remained constant at 2 μL min^{-1}. In other cases, flow rates of both sheath and sample were increased proportionally to maintain a FRR of 50. A LabVIEW program was developed to control the syringe pump and automate data collection from the LCR meter. After the baseline measurements were completed, *E. coli* was passed through the channel and allowed to settle and bind for 20 minutes to the immobilized antibodies. Unbound bacteria were flushed out of the channel, and impedance measurements were conducted. Baseline and *E. coli* experiments were repeated 3 times each and the averages and standard deviations were calculated for each FRR. Resistance and reactance values were extracted from the measured impedance data. The same microchannel was used for baseline and *E. coli* experiments, and the same two sensing electrodes were used in both the 2-electrode and 4-electrode configurations. The cell coverage of the electrode surface area did not change appreciably during the *E. coli* experiments, as judged by microscopic inspection.

Results and discussion

COMSOL simulations and confocal microscopy

Fig. 3a illustrates transverse slices of the COMSOL simulations of a microfluidic channel for FRRs of 25 and 100. Since only half of the channel was simulated, the cross-sections were mirrored and stitched to allow easier comparison with confocal images. All cross-sections were taken 3 mm downstream from sheath inlet. The electrodes are positioned at the bottom surface along the length of the channel. The concentration value of 0 for the nonconductive sheath fluid is shown as blue and the concentration value of 1 for the conductive sample fluid is shown as red.

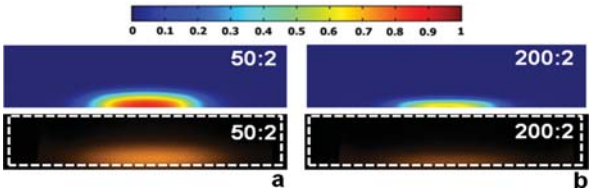

Fig. 3 COMSOL simulations and the corresponding cross-section images from confocal microscopy with a sheath-to-sample flow-rates (in μL min^{-1}) of (a) 50 : 2 and (b) 200 : 2. The same channel was used for the confocal experiment in both cases. The outline shows the boundary of the channel. The diffusion co-efficient for the simulations was 10^9 m^2 s^{-1}. The concentration is specified by the color bar with 0 (blue) as the minimum and 1 (red) as the maximum. The intermediate colors show diffusion region between the sheath and sample streams. The confocal cross-sections were taken 3 mm downstream from the junction where sheath and sample streams met.

The intermediate colors signify the diffusion between the two streams. Fig. 3b shows confocal microscopy images of an actual channel with a 0.25 mm height and 1 mm width. The decrease in image brightness in confocal images is attributed to the diffusion between the sheath and sample fluids.

The channel cross-sections from simulations and confocal images demonstrate how the sheath fluid focused the sample stream from both sides and the top, resulting in a half ellipse-shaped focused stream. Furthermore, both modes of investigation show that an increase in FRR resulted in greater flow focusing toward the electrode surface. The degree of focusing at a specified FRR was roughly the same for both simulations and confocal experiments. The width of the focused stream remained fairly constant due to the geometry of the channel but the change in the height was significant. Thus the effective cross-section of the sample fluid was significantly reduced without minimizing the physical dimensions of the channel.

It is interesting to note that the maximum concentration value in the focused region was smaller for the higher FRR case (FRR = 100) despite the fact that the fluid was flowing faster. In order to understand this effect, consider the simple case of 1D flow focusing at two FRRs: 25 and 100, shown in Fig. 4. The height of the focused layer defined by the boundary between sheath and sample fluids for the two FRR can be estimated by finding the *y*-intercepts of the concentration profiles (Fig. 4a). The diffusion due to flow focusing affected both layers but the maximum concentration in the focused stream was 0.6 for FRR of 100 compared to 0.8 for FRR of 25.

As the FRR became higher, the sample stream was focused more and thus pushed closer to the bottom channel wall. The focused layer heights for FRR of 25 and 100 were roughly 64 μm and 30 μm respectively. The velocity profiles for the flow in the focusing channel are parabolic as shown in Fig. 4b and were used to find the velocities at the sheath–sample boundary using eqn (3). These values turned out to be 4 mm s^{-1} for FRR of 25 and 8.5 mm s^{-1} for FRR of 100. Although the fluid was flowing faster and the residence time was smaller when FRR was 100, the characteristic length over which the diffusion took place was also more significant as compared to focused layer height. Consequently, the *Pe* calculated using the height of the focused stream

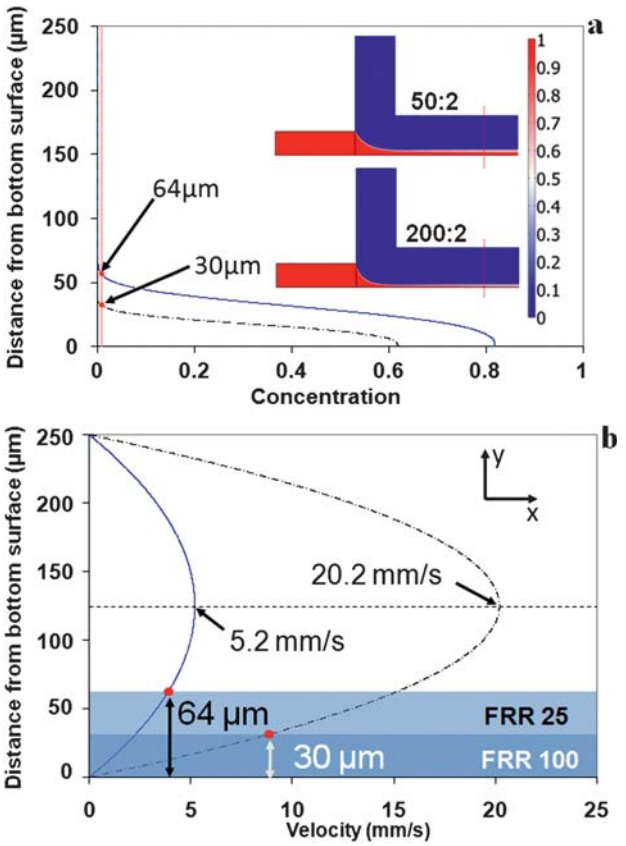

Fig. 4 Flow focusing in a simple 2D model with a 150 μm high sample channel that entering a 250 μm main channel. (a) The inset shows the COMSOL simulations that were used to calculate the concentration profiles along the height of the main channel (solid line 50 : 2 μL min^{-1} and dotted line 200 : 2 μL min^{-1}) 2 mm downstream from T-junction. The heights of the focused layers for two FRRs are taken at points where concentration drops below 0.01. (b) The heights are superimposed on the parabolic velocity profiles for each FRR case to find the actual velocity at which the interface between sheath and sample fluids (v_{x25}, v_{x100}) travels.

as the characteristic length was 250 ± 10 for both FRR but the higher FRR resulted in a smaller cross-sectional stream with lower overall concentration of sample electrolyte. In confocal images, this lowering of sample concentration manifested as a reduction in brightness of the focused region for 200 : 2 μL min^{-1} as compared to 50 : 2 μL min^{-1} (Fig. 3b) and was also accurately predicted by the simulations (Fig. 3a).

Diffusion in parallel laminar flow streams inside microchannels has been studied previously[49–51] and has also been used for biosensing applications.[7,52] However, for impedance sensors that rely on flow-focusing for enhancement of detection sensitivity, this diffusion has deleterious effects. The electric field confinement relies on a sharp gradient between the conducting sample and non-conducting sheath streams. Therefore, any mixing due to transverse diffusion between sheath and sample fluids reduces the confinement of the electric field. The overall effect is a loss in detection sensitivity.

Baseline and *E. coli* measurements

Baseline and *E. coli* measurements were performed using 2- and 4-electrode configurations at different FRRs (25, 50, and 100). The resistance and reactance components of the impedance were measured using the LCR meter, and resistance and capacitance values were extracted assuming parallel RC circuit for the 4-electrode case and series RC circuit for the 2-electrode case (ESI†).

Tables 1 and 2 list mean values and standard deviations of three repeated impedance measurements using the 2- and 4-electrode configurations. The percent change in resistance and capacitance due to the presence of *E. coli* was calculated using

$$\Delta\ (\%) = \left(\frac{E.\ coli - \text{baseline}}{\text{baseline}}\right) \times 100 \qquad (10)$$

For both the 2- and 4-electrode baseline measurements, as the sample fluid became more focused at higher FRRs, the measured resistance values increased. This is expected since the cross-sectional area of the focused stream decreases thus causing an increase in resistance. In addition, resistivity also depends on the number and types of ions in solution. Therefore, the diffusion between the sample and sheath fluids contributed to a further increase in resistance.

For the 2-electrode baseline measurements, the reduction in interfacial capacitance with increased FRR was mostly due to the decrease in the width of the focused stream which effectively decreased the electrode area as described by eqn (4). In the 4-electrode system, the slight decrease in the bulk capacitance was attributed to an increase in cell constant (eqn (9)). As seen from eqn (7), the cell constant is inversely proportional to the focused layer height (eqn (7)) which decreased with increasing FRR.

The resistance and capacitance values with immobilized *E. coli* followed the same trend as the baseline measurements. The presence of *E. coli* caused an increase in the resistance and a decrease in capacitance in both configurations. Bacteria and other cells act as insulators due to the impermeability of cell membrane at low frequencies.[53] The increase in resistance demonstrated that the *E. coli* was insulating and partially blocking the current paths on the electrodes, and thus contributed an additional impedance component to the system. The presence of insulting bacteria resulted in a decrease in capacitance which was due to a decrease in the effective electrode area as per eqn (4). The two-electrode system was more sensitive to changes at the electrode surface, as is highlighted by a greater change in capacitance due to the presence of the *E. coli* cells on the electrodes.

Interestingly, when the FRR was increased, the % change in resistance and capacitance decreased. This effect is attributed to the diffusion of ions from the conducting stream into the non-conducting sheath fluid. As shown earlier, the amount of diffusion was roughly the same, but the characteristic length over which the diffusion occurred became more significant as the cross-sectional area of the focused stream decreased. This increased the bulk resistance and competed with the insulating effect of the *E. coli.* The overall effect was a decrease in % change in resistance as FRR increased. From eqn (6) and (9), it can be seen that an increase in resistivity also caused an increase in the capacitance which counteracted the decrease in capacitance due to presence of cells on the electrodes. Overall, the % change in capacitance decreased slightly as FRR was increased. Thus as the sample fluid became more focused, the diffusion had more impact on the measured data (also seen in Fig. 3).

Table 1 Baseline and *E. coli* resistance and capacitance values for the 2-electrode configuration sensor

	Bulk resistance, R/kΩ			Interfacial capacitance, C/nF		
FRR	Baseline	*E. coli*	Δ (%)	Baseline	*E. coli*	Δ (%)
50 : 2	33.1 ± 0.6	37.5 ± 0.3	13.5	16.2 ± 1.0	14.0 ± 1.0	−13.9
100 : 2	52.9 ± 0.8	58.8 ± 0.5	11.2	12.4 ± 0.1	11.1 ± 0.1	−10.2
200 : 2	79.3 ± 0.7	85.6 ± 2.2	8.0	9.2 ± 0.1	9.0 ± 0.2	−2.3

Table 2 Baseline and *E. coli* resistance and capacitance values for the 4-electrode configuration sensor

	Bulk resistance, R/kΩ			Bulk capacitance, C/nF		
FRR	Baseline	*E. coli*	Δ (%)	Baseline	*E. coli*	Δ (%)
50 : 2	31.5 ± 0.7	38.1 ± 1.0	20.8	1.36 ± 0.02	1.31 ± 0.02	−3.7
100 : 2	53.0 ± 0.5	61.2 ± 0.2	15.6	1.29 ± 0.01	1.26 ± 0.01	−2.3
200 : 2	78.6 ± 1.3	90.3 ± 0.9	14.8	1.20 ± 0.01	1.18 ± 0.01	−1.7

The amount of diffusion between the sheath and sample is dictated by the residence time or the time sheath and sample streams are in contact with each other and the distance over which transverse diffusion takes place. As the FRR increased, fluid flowed faster in the channel and decreased the residence time and, therefore, the diffusion of the ions out of the sample fluid. At the same time, increasing the FRR pushed the focused stream closer to the channel wall decreasing the mean distance of an ion to the sample–sheath interface.

In order to delineate these two phenomena, confocal microscopy, simulations and impedance measurements were performed for cases with same FRR but with increasing sheath and sample flow velocities. As the fluid flowed faster, the residence time decreased and resulted in less diffusion within a fixed distance. Fig. 5a shows confocal images of sample only, and sheath-to-sample flow rates of 50 : 1, 100 : 2 and 200 : 4 μL min^{-1}. All three cases have FRR equal to 50; however, the sheath and sample fluids of the 200 : 4 ratio were flowing 4-times faster (13.6 mm s^{-1}).

Both confocal images and simulations show that there was relatively little change in focused stream height since the FRR was unchanged. The results also showed that more diffusion occurred when the fluids were flowing slower, as signified by the loss in brightness of the focused region at slower flow velocities. COMSOL simulation results (Fig. 5b) further confirmed this finding. Based on the results shown in Fig. 3 and 5, it is clear that in order to improve the detection sensitivity, without introducing the deleterious effects of diffusion, both the FRR and absolute flow velocities must be increased simultaneously.

It should be noted, however, that there was an upper bound for sheath and sample flow velocities beyond which any increase in flow velocities caused the inertial forces to become significant and simultaneously started changing the way sheath focused the sample stream for the particular channel design used in this investigation. As seen at highest flow velocities in Fig. 5a (200 : 4 μL min^{-1}) and 5b (500 : 10 μL min^{-1}), as the *Re* increased, the sheath stream lost its ability to focus the sample stream from the sides and this resulted in widening of the focused stream along the bottom surface of the channel wall. A further increase in the flow velocities led to the splitting of the sample stream into two focused streams. The optimal condition for this design to provide maximum focusing but with the least effect of diffusion appears to be sheath-to-sample flow rates of 100 : 2 μL min^{-1} (FRR = 50 and *Re* = 2.7). The diffusion between sheath and sample fluid can also be reduced by using ionic species with slower diffusion coefficients or by using fluids that are immiscible *i.e.* two-phase. However, two-phase parallel flows are only possible in narrow FRR regime.[54]

Impedance measurements were performed at FRRs of 25 and 50 using the 4-electrode configuration. The sample flow rates steps were 2, 4, 8, and 16 μL min^{-1}, and the sheath flow rates were increased accordingly to obtain the corresponding FRR. The FRRs were maintained for 30 s at each step and the values were averaged over the step. The plot in Fig. 6 shows that the resistance decreased as flow velocities increased due to a decrease in diffusion. The values of capacitances were largely unaffected for the 4-electrode configuration.

Conclusions

A 2D flow focusing technique was implemented for a modified T-junction design. Two- and four-electrode configurations for impedance measurements were characterized for detection sensitivity. Measuring a change in resistance using the 4-electrode configuration was the most sensitive technique to detect the presence of *E. coli* at low frequencies in a flow focusing system. The 2-electrode technique showed a greater % change in capacitance than the 4-electrode sensor because the cells were bound to the electrode surface and the 2-electrode configuration is more sensitive to changes at the electrode interface. The fact that the % change in impedance decreased with increasing FRRs indicated that the presence of the bacteria became less significant with increased focusing, even though they represented a higher proportion of the cross-sectional area of the conducting stream. This effect was attributed to the increased effect of the diffusion of ions out of the focused stream as the focused stream height decreased. One way to reduce diffusion was to increase the actual sheath and sample flow velocities in addition to increasing the FRR. Diffusion must be properly controlled in order to prevent

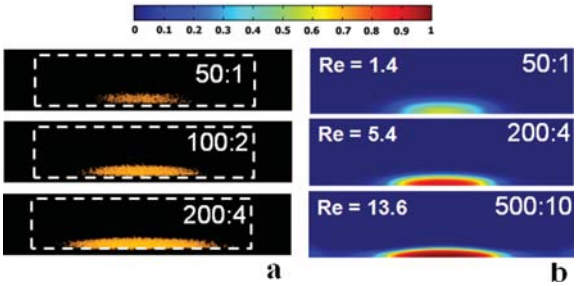

Fig. 5 (a) Confocal images for sheath-to-sample flow rates (in μL min^{-1}) of 50 : 1, 100 : 2 and 200 : 4 (FRR = 50) are shown. The contrast was adjusted by same measure for all cross-sections to allow easier visualization of focused stream. (b) Channel cross-sections show concentration distributions from COMSOL simulations. Flow velocities of both sheath and sample streams were increased proportionally to maintain the FRR at 50. The diffusion coefficient was 1×10^{-9} m^2 s^{-1} for all cases. The concentrations are specified by the color bar with 0 (blue) as the minimum and 1 (red) as the maximum.

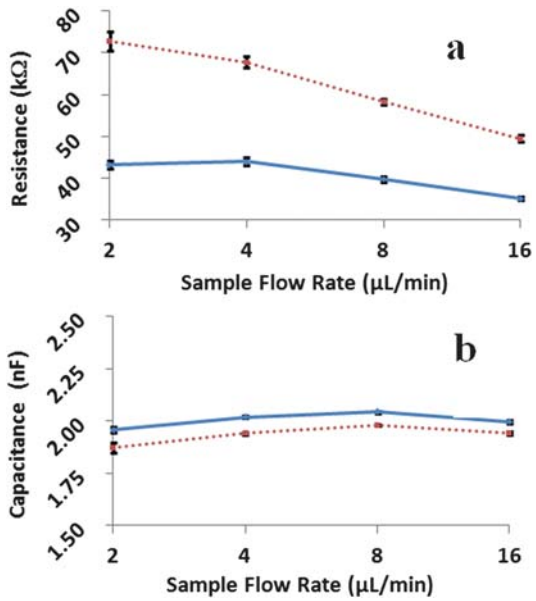

Fig. 6 Sample and sheath flow rates were increased while keeping the FRRs constant (---■--- = FRR of 50, —◆— = FRR of 25). Sheath flow rates are: FRR × sample flow rate. A 4-electrode configuration was used to measure (a) resistance and (b) capacitance.

a loss in detection sensitivity using flow focusing and impedance measurements.

Acknowledgements

This project is funded by the Defense Threat Reduction Agency (DTRA #AA07CBT015). The authors would like to thank Dr G. Justin, Dr D. Mott and Dr Stanislav Tsoi at NRL, and Dr Shekhar Bhansali at the University of South Florida for discussions. Mansoor Nasir was a National Research Council (NRC) Postdoctoral Fellow. The views are those of the authors and do not represent the opinion or policy of the US Navy or Department of Defense.

References

1 P. Leonard, S. Hearty, J. Brennan, L. Dunne, J. Quinn, T. Chakraborty and R. O'Kennedy, *Enzyme Microb. Technol.*, 2003, **32**, 3–13.
2 P. D. Patel, *TrAC, Trends Anal. Chem.*, 2002, **21**, 96–115.
3 K. R. Rogers, *Anal. Chim. Acta*, 2006, **568**, 222–231.
4 J. Wang, *Anal. Chim. Acta*, 2004, **507**, 3–10.
5 A. P. Turner, *Science (New York, NY)*, 2000, **290**, 1315.
6 J. P. Brody and P. Yager, *Sens. Actuators, A*, 1997, **58**, 13–18.
7 A. Hatch, A. E. Kamholz, K. R. Hawkins, M. S. Munson, E. A. Schilling, B. H. Weigl and P. Yager, *Nat. Biotechnol.*, 2001, **19**, 461–465.
8 T. Stiles, R. Fallon, T. Vestad, J. Oakey, D. W. M. Marr, J. Squier and R. Jimenez, *Microfluid. Nanofluid.*, 2005, **1**, 280–283.
9 P. A. Walsh, E. J. Walsh and M. R. D. Davies, *Int. J. Heat Fluid Flow*, 2007, **28**, 44–53.
10 D. Huh, W. Gu, Y. Kamotani, J. B. Grotberg and S. Takayama, *Physiol. Meas.*, 2005, **26**, 73.
11 E. Brooks Shera, N. K. Seitzinger, L. M. Davis, R. A. Keller and S. A. Soper, *Chem. Phys. Lett.*, 1990, **174**, 553–557.
12 G. B. Lee, C. I. Hung, B. J. Ke, G. R. Huang, B. H. Hwei and H. F. Lai, *J. Fluids Eng.*, 2001, **123**, 672–679.
13 J. H. Nieuwenhuis, F. Kohl, J. Bastemeijer, P. M. Sarro and M. J. Vellekoop, *Sens. Actuators, B*, 2004, **102**, 44–50.
14 A. Wolff, I. R. Perch-Nielsen, U. D. Larsen, P. Friis, G. Goranovic, C. R. Poulsen, J. P. Kutter and P. Telleman, *Lab Chip*, 2003, **3**, 22–27.
15 J. B. Knight, A. Vishwanath, J. P. Brody and R. H. Austin, *Phys. Rev. Lett.*, 1998, **80**, 3863–3866.
16 S. H. Wong, M. C. L. Ward and C. W. Wharton, *Sens. Actuators, B*, 2004, **100**, 359–379.
17 J. P. Golden, C. R. Taitt, L. C. Shriver-Lake, Y. S. Shubin and F. S. Ligler, *Talanta*, 2005, **65**, 1078–1085.
18 H. Fricke, *J. Gen. Physiol.*, 1925, **9**, 137.
19 H. P. Schwan and K. S. Cole, Bioelectricity: alternating current admittance of cells and tissues, in Medical Physics, Chicago, Yearbook Publishers, Inc., 1960, **vol. 3**, 52–56.
20 R. Gomez, R. Bashir, A. Sarikaya, M. R. Ladisch, J. Sturgis, J. P. Robinson, T. Geng, A. K. Bhunia, H. L. Apple and S. Wereley, *Biomed. Microdevices*, 2001, **3**, 201–209.
21 S. Gawad, L. Schild and P. Renaud, *Lab Chip*, 2001, **1**, 76–82.
22 I. Giaever and C. R. Keese, *Proc. Natl. Acad. Sci. U. S. A.*, 1991, **88**, 7896–7900.
23 S. Z. Hua and T. Pennell, *Lab Chip*, 2009, **9**, 251–256.
24 U. D. Larsen, G. Blankenstein and J. Branebjerg, *Transducers '97, 1997 International Conference on Solid State Sensors and Actuators, Chicago*, 1997, pp. 1319–1322.
25 R. Rodriguez-Trujillo, O. Castillo-Fernandez, M. Garrido, M. Arundell, A. Valencia and G. Gomila, *Biosens. Bioelectron.*, 2008, **24**, 290–296.
26 C. Simonnet and A. Groisman, *Anal. Chem.*, 2006, **78**, 5653–5663.
27 S. Kostner and M. J. Vellekoop, *Sens. Actuators, B*, 2008, **132**, 512–517.
28 T. Sun, D. Holmes, S. Gawad, N. G. Green and H. Morgan, *Lab Chip*, 2007, **7**, 1034–1040.
29 T. Sun and H. Morgan, *Microfluid. Nanofluid.*, 2010, **8**, 1–21.
30 E. T. McAdams, A. Lackermeier, J. A. McLaughlin, D. Macken and J. Jossinet, *Biosens. Bioelectron.*, 1995, **10**, 67–74.
31 T. York, *Journal of Electronic Imaging*, 2001, **10**, 608.
32 H. P. Schwan, *Ann. N. Y. Acad. Sci.*, 1968, **148**, 191–209.
33 R. Bragós, E. Sarró, A. Fontova, A. Soley, J. Cairó, A. Bayés-Genís and J. Rosell, *Annual International Conference of the IEEE Engineering in Medicine and Biology Society*, 2006, p. 2106.
34 M. Nasir, D. A. Ateya, D. Burk, J. P. Golden and F. S. Ligler, *Biosens. Bioelectron.*, 2010, **25**, 1363–1369.
35 R. H. Liu, M. A. Stremler, K. V. Sharp, M. G. Olsen, J. G. Santiago, R. J. Adrian, H. Aref and D. J. Beebe, *J. Microelectromech. Syst.*, 2000, **9**, 190–197.
36 J. Atencia and D. J. Beebe, *Nature*, 2005, **437**, 648–655.
37 F. M. White, *Viscous Fluid Flow*, 1991, McGraw-Hill, New York, pp. 105–217.
38 J. Hong, D. S. Yoon, M. I. Park, J. Choi, T. S. Kim, G. Im, S. Kim, Y. E. Pak and K. No, *Jpn. J. Appl. Phys.*, 2004, **43**, 5639–5645.
39 A. J. Bard and L. R. Faulkner, *Electrochemical Methods*, Wiley, New York, 2001.

40 G. R. Langereis, *An integrated sensor system for monitoring washing processes*, *PhD Thesis*, Enschede, University of Twente, ISBN 90-365-1272-7, 1999.
41 A. Ivorra, in *Electronic Engineering Department*, Universitat Politècnica de Catalunya, Barcelona, 2005, p. 224.
42 P. N. Robillard and D. Poussart, *IEEE Trans. Biomed. Eng.*, 1979, **8**, 465–470.
43 P. Linderholm, T. Braschler, J. Vannod, Y. Barrandon, M. Brouard and P. Renaud, *Lab Chip*, 2006, **6**, 1155–1162.
44 J. B. Hasted, D. M. Ritson and C. H. Collie, *J. Chem. Phys.*, 1948, **16**, 1.
45 R. A. Robinson and R. H. Stokes, *Electrolyte Solutions*, Dover Publications, 2002.
46 W. Olthuis, W. Streekstra and P. Bergveld, *Sens. Actuators, B*, 1995, **24**, 252–256.
47 D. M. Leatzow, J. M. Dodson, J. P. Golden and F. S. Ligler, *Biosens. Bioelectron.*, 2002, **17**, 105–110.
48 M. P. Chatrathi, J. Wang and G. Collins, *Biosens. Bioelectron.*, 2007, **22**, 2932–2938.
49 A. E. Kamholz, B. H. Weigl, B. A. Finlayson and P. Yager, *Anal. Chem.*, 1999, **71**, 5340–5347.
50 R. Yang, D. L. Feeback and W. Wang, *Sens. Actuators, A*, 2005, **118**, 259–267.
51 R. F. Ismagilov, A. D. Stroock, P. J. A. Kenis, G. Whitesides and H. A. Stone, *Appl. Phys. Lett.*, 2000, **76**, 2376.
52 B. H. Weigl and P. Yager, *Science*, 1999, **283**, 346.
53 H. P. Schwan and C. F. Kay, *Ann. N. Y. Acad. Sci.*, 1957, **65**, 1007.
54 P. Guillot and A. Colin, *Phys. Rev. E: Stat., Nonlinear, Soft Matter Phys.*, 2005, **72**, 66301.